



Impact fatigue damage of coated glass fibre reinforced polymer laminate

Fraisse, Anthony; Bech, Jakob Ilsted; Borum, Kaj Kvisgaard; Fedorov, Vladimir; Johansen, Nicolai Frost-Jensen; McGugan, Malcolm; Mishnaevsky, Leon; Kusano, Yukihiro

Published in:
Renewable Energy

Link to article, DOI:
[10.1016/j.renene.2018.04.043](https://doi.org/10.1016/j.renene.2018.04.043)

Publication date:
2018

Document Version
Peer reviewed version

[Link back to DTU Orbit](#)

Citation (APA):

Fraisse, A., Bech, J. I., Borum, K. K., Fedorov, V., Johansen, N. F-J., McGugan, M., Mishnaevsky, L., & Kusano, Y. (2018). Impact fatigue damage of coated glass fibre reinforced polymer laminate. *Renewable Energy*, 1102-1112. <https://doi.org/10.1016/j.renene.2018.04.043>

General rights

Copyright and moral rights for the publications made accessible in the public portal are retained by the authors and/or other copyright owners and it is a condition of accessing publications that users recognise and abide by the legal requirements associated with these rights.

- Users may download and print one copy of any publication from the public portal for the purpose of private study or research.
- You may not further distribute the material or use it for any profit-making activity or commercial gain
- You may freely distribute the URL identifying the publication in the public portal

If you believe that this document breaches copyright please contact us providing details, and we will remove access to the work immediately and investigate your claim.

1 Impact fatigue damage of coated glass fibre 2 reinforced polymer laminate 3

4 Anthony Fraisse¹, Jakob Ilsted Bech¹, Kaj Kvisgaard Borum¹, Vladimir Fedorov¹, Nicolai Frost-Jensen
5 Johansen², Malcolm McGugan¹, Leon Mishnaevsky Jr.¹, Yukihiro Kusano¹

6 ¹Department of Wind Energy, Technical University of Denmark, Risø Campus, 4000 Roskilde, Denmark

7 ²Department of Mechanical Engineering, Technical University of Denmark, Lyngby Campus, 2800 Lyngby,
8 Denmark

9

10 **Abstract.** Impact fatigue caused by rain droplets, also called rain erosion, is a severe problem for wind turbine blades
11 and aircraft. In this work, an assessment of impact fatigue on a glass fibre reinforced polymer laminate with a gelcoat is
12 presented and the damage mechanisms are investigated. A single point impact fatigue tester is developed to generate
13 impact fatigue damage and SN data. Rubber balls are repeatedly impacted on a single location of the coated laminate.
14 Each impact induces transient stresses in the coated laminate. After repeated impacts, these stresses generate cracks,
15 leading to the removal of the coating and damage to the laminate. High-resolution digital imaging is used to determine
16 the incubation time until the onset of coating damage, and generate an SN curve. An acoustic emission sensor placed at
17 the back of the laminate monitors changes in acoustic response as damage develops in the coated laminate. The subsurface
18 cracks are studied and mapped by 3D X-ray computed tomography. A finite element method model of the impact shows
19 the impact stresses in the coating and the laminate. The stresses seen in the model are compared to cracks found by 3D
20 tomography. The damage is also evaluated by ultrasonic scanning.

21

22 Keywords: Impact fatigue; glass fibre reinforced polymer; leading edge erosion; acoustic emission; X-ray computed
23 tomography; ultrasound scanning

24

25

26 1. Introduction

27

28 Wind energy is recognized as a key renewable energy source, reducing dependency on fossil fuels [1, 2, 3, 4].
29 There are a variety of designs for energy generation by wind, but in all cases, the kinetic energy of wind is
30 converted to electrical energy. The three bladed horizontal axis wind turbine is a common design, comprising
31 rotor blades, a tower and a power converting part including a generator and a gear box. Since the power
32 generation capacity of a wind turbine highly depends on the swept area of the blades, lighter and larger blades
33 are demanded [5, 6]. Fibre reinforced polymer composite materials can meet the demand for lighter and larger
34 wind turbine blades due to their high strength-to-mass ratio, a high stiffness-to-mass ratio, good fatigue
35 resistance, corrosion resistance, flexible formability and low thermal expansion.

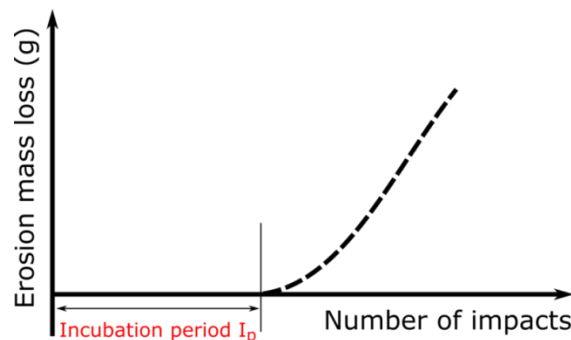
36 Surfaces of wind turbine blades in both onshore- and offshore-installations are exposed environmental and
37 tribological effects over their operational lifetimes [7], including extreme wind/gusts, rain showers, hailstone
38 showers, airborne particles of sand, snow, icing, extreme temperatures and ultraviolet light exposure. Among
39 them rain erosion is often thought to be a major damage source [8]. In particular, the leading edge of the blade
40 tips, whose speed is commonly greater than 80 m s^{-1} [9], can experience significant damage, and thus a
41 protective coating is usually applied. Such damages are collectively called “leading edge erosion”. However,
42 erosion is only one of the damage phenomena, and in fact, very little is known about the different damage

43 modes and mechanisms. All wind farms require frequent visual inspection of the blades and subsequent repair
44 or replacement due to unpredictable damages.

45 Attempts to reproduce the rain erosion damage phenomena in laboratory scale can be found in literature eg
46 [10]. Rain erosion testing (RET) is used to experimentally assess rain erosion performances. The most common
47 test for rain erosion in wind energy applications is the rotating arm rig, where a rotor is rotating in a rain field
48 of generated droplets [11]. It was originally developed for aerospace materials. Despite the prevalence of this
49 test method there is a problem in reproducibility when different test setups are compared. This is mainly due
50 to turbulence in the test rigs, different droplet size distributions, and other parameters which are difficult to
51 control. In addition, the evaluation mainly relies on visual inspection of the protective coatings to document
52 damage and delamination, and a measurement of the material mass loss, without taking account of damage
53 modes. The testing requires these operation to be stopped and the blade sample unmounted, making
54 observation limited to few discrete intervals, and an observation of exact failure times and mechanisms
55 difficult. Considering these circumstances, development of a highly controlled impact test method, in-situ
56 monitoring and damage characterisation techniques are needed for studying the impact damage mechanisms
57 in detail. Impact damage and impact fatigue are also studied by other means like drop weight tests and shooting
58 with projectiles [12].

59 The effect of repeated mechanical loading in a material's lifetime has been studied based on a concept of
60 cumulative fatigue damages [13, 14]. This concept can be applied to the impact fatigue damage of coated
61 systems. There is usually an initial incubation period during which damage accumulates in the material while
62 no visible damage and no functional loss is detected, as shown in Figure 1. After the incubation period, a steady
63 damage evolution may be measured. For the leading edge erosion of wind turbine blades, a delta mass method
64 is commonly used, in which mass loss of a material is measured at discrete time intervals. With this method,
65 the impact damage process may be simplified to two discrete stages. In the incubation period, small cracks
66 begin to form inside the material and each crack further extends as the impacts continue. At some point, the
67 cumulative damage results in cracks merging and an initial removal of a portion of the material at the surface,
68 followed by a period of steady mass loss. Drawbacks of the delta mass methods are that in-situ measurements
69 are difficult to perform due to severe mechanical impacts and the fact that initial damages including crack
70 creation are not detected. Therefore, it is desirable to use enhanced inspection techniques suitable for in-situ
71 observation and monitoring, such as visual imaging and acoustic detection.

72



73

74 Figure 1. Schematic diagram of erosion mass loss as a function of the number of impacts, accompanying an
75 incubation period I_p at the initial stage of impacts.

76

77 In the present work, a newly developed single point impact fatigue test (SPIFT) is presented. Ex-situ
78 measurements of ultrasonic scanning and X-ray tomography were performed to identify initial defects in
79 specimens. After that, the impact fatigue test was carried out. Rubber balls are used to impact specimen
80 surfaces with a defined impact-speed and interval. During the impact test, the specimen surface was observed
81 in-situ by digital imaging, and acoustic signals were measured. After the impacts, the specimens were again

82 characterised by the ex-situ methods for damage analysis. The results were compared with stress wave
83 propagation in the specimen simulated by a finite element method (FEM) model.

84

85

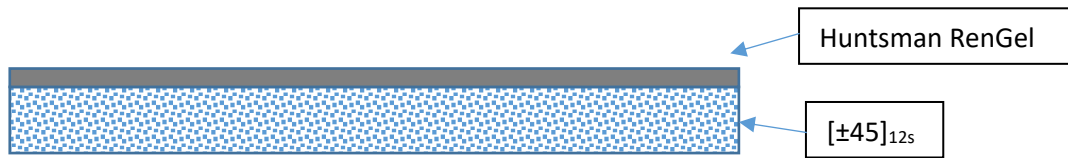
86 2. Experimental setup and methods

87

88 2.1. Materials

89 Flat glass fibre reinforced polymer (GFRP) laminates coated with an epoxy based gelcoat were manufactured
90 by vacuum infusion as shown in Figure 3. The uncured gelcoat layer (Huntsman, RenGel, SW 5200 / Ren NY
91 5212, density = 1.5 g cm^{-3}) was first placed on a flat mould surface, on which fibre fabric layers were placed
92 in addition to process aid foils. The symmetric fibre layup was established using twelve fabric layers. The
93 fabric layers in the lay-up were biaxial ($\pm 45^\circ$) 444 g m^{-2} layers (Saertex, density = 2.60 g cm^{-3}). A Huntsman
94 epoxy resin (epoxy: LY 1564 SP, hardener: Aradur 3487. Huntsmann) was infused into the mould to
95 impregnate the fibres. Panels were cured at 40°C for 21 h and post-cured at 80°C for 5 h.

96



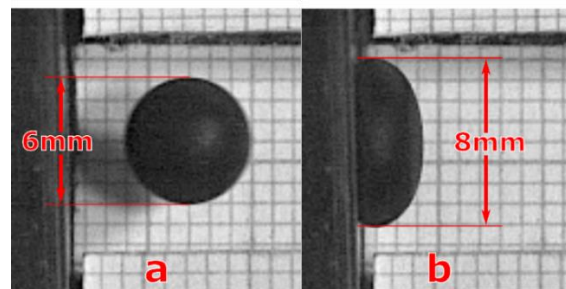
97 Figure 3. Material lay-up.

98

99 2.2. Projectile material

100 The projectiles used for impact testing are $\text{Ø}6 \text{ mm}$ balls made from Buna nitrile rubber (NBR60), with a shore
101 hardness of 60. The mass of each ball is 0.143 g giving each ball a density of 1.267 kg m^{-3} . The choice of
102 NBR60 for the projectiles is based on the need for a low-modulus material that would remain intact during
103 repeated impacts, while still having a density close to that of water. In order to reduce friction between the
104 barrel and the rubber ball while firing, a small amount of silicon oil lubrication was used to coat the rubber
105 balls. Figure 4 shows the projectile deforming upon impact with the target. Using high-speed imaging to
106 visualise this deformation, it can be seen that the degree of deformation is dependent upon impact speed,
107 ranging from $\text{Ø}6.9 \text{ mm}$ at 88 m s^{-1} to $\text{Ø}8 \text{ mm}$ at 167 m s^{-1} .

108



109

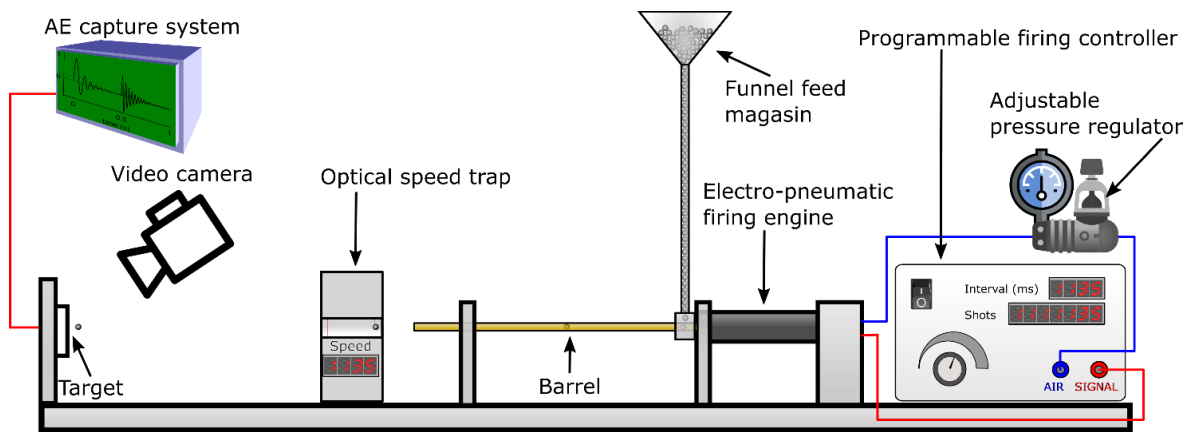
110 Figure 4. High-speed imaging of the 6 mm rubber balls captured using a Phantom v2512-fast high-speed
111 camera at 38016 fps $2.1\mu\text{s}$ exposure time. (a) just before impact travelling at 167.02 m s^{-1} . (b) the deformed
112 projectile at $\text{Ø}8 \text{ mm}$, $26.15 \mu\text{s}$ after the initial impact.

113

114 2.3. *Single point impact fatigue tester (SPIFT)*

115 The SPIFT repeatedly shoots rubber balls at a coated $15 \times 40 \times 5 \text{ mm}^3$ laminate. The shooter is a Valken V12
116 electro-pneumatic firing engine, driven by compressed air and containing a plunger and two magnetic valves.
117 The schematic setup is illustrated in Figure 5. The balls are fed by gravity into the firing mechanism from a
118 vibrating magazine hopper. The plunger lets the balls into the chamber one by one. After entering the chamber
119 the rubber ball is loaded into the barrel, whereupon compressed air is released to accelerate the rubber ball
120 through the barrel. After leaving the barrel the rubber ball passes through an optical speed trap (Airchrony
121 Mk.3) recording the exit velocity of the rubber ball. Having passed the speed trap the rubber ball hits the target.
122 The setup can shoot up to 5 rubber balls per second with velocities up to 170 m s^{-1} . The velocity is regulated
123 by the applied air pressure. The time interval between shots and the number of shots in a series are controlled
124 by a programmable microprocessor giving input to the magnetic valves. During testing the impact area is
125 monitored using a digital microscope camera.

126



127

128 Figure 5. SPIFT setup.

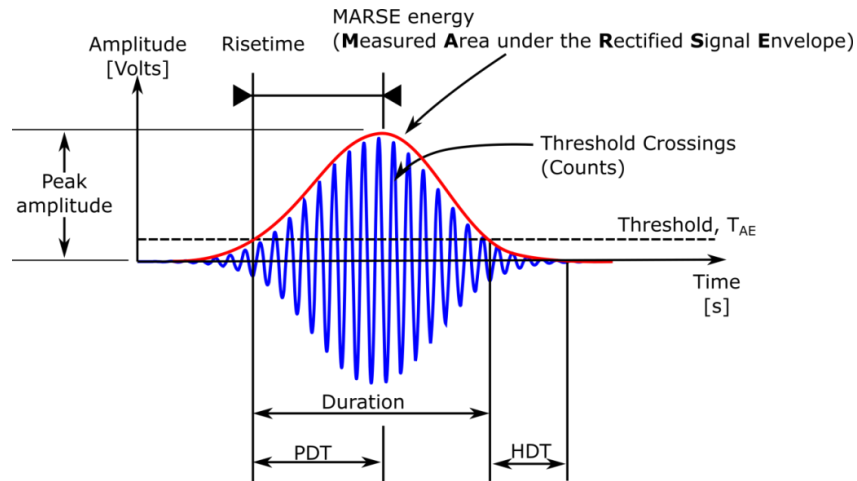
129

130 2.4. *Digital video acquisition*

131 As the primary means of damage detection, high-resolution digital video images were captured at a 3.1
132 Megapixel ($2048 \times 1534 @ 10\text{Hz}$) with an AM7915MZTL long working distance USB microscope from Dino-
133 lite. Using a working distance of 120 mm, a $18 \times 13 \text{ mm}^2$ field of view is obtained resulting in $13.5 \text{ pixels mm}^{-2}$.
134

135 2.5. *Acoustic emission*

136 Acoustic Emission (AE) refers to the elastic stress wave energy that travels through a material when it cracks,
137 or an impact takes place, or some other process occurs that imparts or releases mechanical energy into the
138 system. That energy then travels through the material and can be detected by surface mounted sensors. When
139 the transient energy generated by an impact (as in this case) reaches a surface-mounted AE sensor, the micro
140 accelerations activate the piezoelectric crystal inside the sensor. The fluctuating charge of the piezoelectric
141 crystal is then amplified and the resulting waveform is delivered to the AE system which digitises and
142 processes the information.



143

144 Figure 6. Amplified waveform schematically showing timing parameters and extracted AE features.

145

146 In order to extract relevant features from the transient waveform, user defined detection and timing parameters
 147 must be provided as illustrated in Figure 6. These include a threshold voltage (T_{AE}) above which an AE “hit”
 148 will be registered, a Peak definition time (PDT) specifying the time allowed after the detection of a “hit”
 149 to determine the peak value for that hit – if PDT is too long then false peak values are likely to be recorded. If
 150 too short, the true value may not be identified. Other timing parameters like hit definition time (HDT) and hit
 151 lockout time (HLT) must also be specified and can likewise result in incorrect waveform characterization if
 152 set incorrectly.

153 With an AE sensor on the SPIFT specimen we will register the stress wave response resulting from each
 154 individual impact event; an impact detection. In addition we hope, by comparing changes in the extracted AE
 155 waveform features, to show an impact characterisation that will discriminate between different velocities and
 156 different laminate material, specimen dimensions and attachment/mountings, different coating/protection
 157 layers, and ultimately the damage state (of both coating and laminate).

158 Figure 5 in section 2.3 shows the SPIFT setup with a single AE sensor attached to the reverse side of the coated
 159 laminate. A laboratory optimised Express-8 AE board and chassis system from Mistras Group¹ was used to
 160 detect and analyse the signals. As only a small space was available for instrumentation, a miniature Pico sensor²
 161 was used.

162 With the sensor in place and the system running a problem became apparent. Each rubber ball impact resulted
 163 in multiple AE “hits” being detected. Altering the user defined detection and timing configuration to the
 164 following (Threshold 50 dB, PDT 150 μ s, HDT 1500 μ s and HLT 1500 μ s) solved this issue and thereafter the
 165 system recorded a unique individual AE event for every impact occurring.

166 2.6. *Ultrasound scanning*

167 Ultrasound refers to sound waves, traveling through a material with a frequency far higher than the audible
 168 limit of human hearing. For material evaluation, a typical frequency range is defined between 1 and 50 MHz.
 169 For high resolution measurements, the test was conducted in water using a focused transducer.

170 A focused ultrasonic wave was sent into the material by the transducer and reflections from interfaces were
 171 recorded by the same transducer (Figure 7).

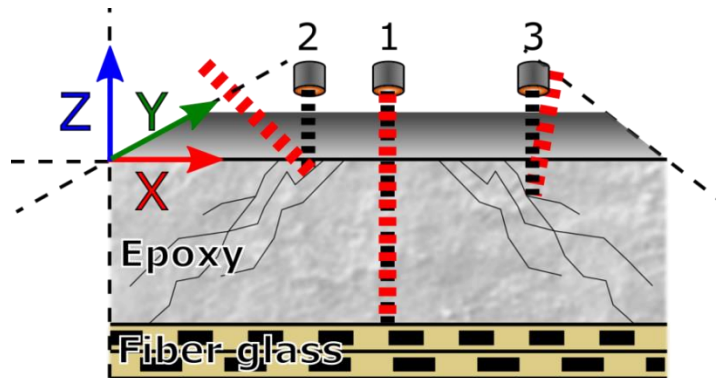
¹ <http://www.physicalacoustics.com/by-product/micro-ii-express/>

² http://www.physicalacoustics.com/content/literature/sensors/Model_PICO.pdf

172 Each solid material and liquid has its own specific ultrasonic impedance Z . In linear elastic materials, the
 173 impedance is a function of the material density (ρ) and the sound speed of sound c in the given material, $Z =$
 174 $\rho \cdot c$. If the ultrasonic wave meets a different material with a different impedance, the ultrasonic wave will be
 175 partly reflected. The larger the difference between the impedance of the two materials, the larger the energy
 176 reflection. Therefore, voids or cracks perpendicular to the wave are relatively easy to detect using ultrasound
 177 due to the large difference in impedance between air and solid material. The scanner probe was mounted on a
 178 gantry that moved in X-Y-Z-planes controlled by stepper-motors. The resulting line scans were combined into
 179 a 2D raster image. At each raster point, an ultrasonic wave was sent into the material and the response was
 180 recorded. The resulting scan may be presented as a 2D contour plot showing local properties using a colour-
 181 scale.

182 There are three scenarios describing the wave interaction with defects. In the first one (1), the ultrasound
 183 waves are reflected directly back from the laminate. Since the surface is normal to the sensor, the intensity of
 184 the reflected echo is strong. In scenarios 2 and 3 most of the ultrasonic wave is reflected at an angle which
 185 gives a weak response to the sensor. Table 1 summarises the parameters selected for the ultrasound scanning.

186



187

188 Figure 7. Scenarios of ultrasound interaction with defects. See the main text for further details.

189

190 Table 1. Ultrasound parameters.

Transducer frequency	Scan resolution X and Y	Distance from transducer to sample surface
50 MHz (focused, 0.2 mm 6 dB limit)	0.1 mm for full sample, 0.02 mm for zoom scan	15.3 mm

191

192 2.7. 3D X-ray computed tomography

193 In the X-ray scanner, the specimen is placed between an X-ray source and a detector. The intensity of the
 194 radiation reaching the sensor depends on the density of the material. The sensor has a number of
 195 “pixels/sensors” each getting charged by the X-ray transmitted through the specimen during the exposure.
 196 Thus a 2D image presenting the variation of damping in the specimen is generated. By gradually turning 180°
 197 and scanning for each few degrees a number of 2D images are generated, each presenting a plane in the scanned
 198 volume. Using Computerized tomography a 3D matrix of the damping in each scanned volume is generated.
 199 Using imaging software any plane/slice of the scanned volume can be carefully evaluated. The software
 200 permits both an investigation of each of the 2D planes from the 3 directions, as well as presenting the overall
 201 3D volume.

202 The X-ray scans were performed using a Zeiss Xradia 520 Versa. This device can scan a specimen with a
 203 characteristic size up to 10 cm with a resolution 100 μm and smaller samples with a resolution down to less

204 than 1 μm . In this study, the sample size was defined to be 15 mm wide and 40 mm long. This geometry has
 205 been defined in order to have a representative volume of the material to test and to ensure a good scan quality.
 206 3D ex-situ tomography was chosen as the characterisation technique for its nondestructive aspect and capacity
 207 to identify and follow the damage mechanisms in the coated laminate during impact fatigue. The repeatability
 208 of the method can be a challenge, and therefore special care was taken while mounting the samples in the
 209 scanner. As shown in Figure 8, a hole was drilled in the sample in which a pin was inserted to precisely index
 210 the specimen for each scan.

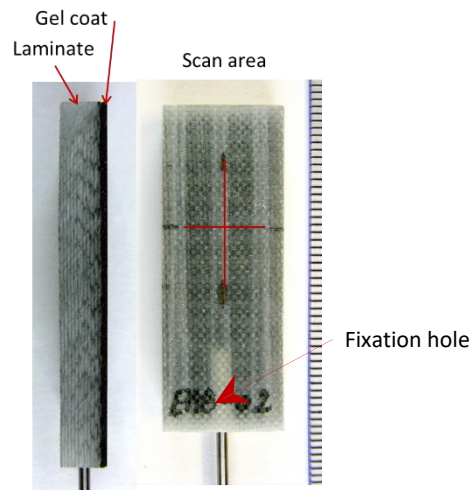
211 The 3D scans shown in this study were obtained using the parameters gathered in Table 2.

212

213 Table 2. Scan parameters.

Objective	Binning	Exposure time (s)	Filtre	Voltage (kV)	Field of view (mm)	Distance to detector (mm)	Distance to source (mm)	Scan rotation (deg)	Number of projections
X4	2	14	LE4	55	2.04	40	17	360	5201

214



215 Figure 8. The coated laminate with mounted pin.

216

217 2.8. *FEM model*

218 An FEM of impact onto the coated laminate was developed to study internal transient stresses. Two models
 219 were developed: One for a rubber ball, and another for a water droplet impacting the coated laminate. Since
 220 the impact process implies a large particle and local laminate deformations, a special finite element
 221 configuration was developed. The target laminate was modelled using the commonly used Eulerian domain,
 222 where each finite element corresponds to the specific material particles. The projectiles (rubber ball and water
 223 droplet) were specified in the Lagrangian domain, where the material was not fixed to the mesh but flew
 224 through it. The finite models were developed in ABAQUS which allows for combinations and interactions of
 225 Eulerian and Lagrangian domains in the same model.

226 The model consists of a target laminated with 12 uni-directional 0.6 mm thick glass-fibre layers and a 1.1 mm
 227 thick gelcoat layer on top of the laminate, reproducing the laminate used for the experiments (Figure 3). The
 228 projectiles are 6 mm diameter balls approaching the target laminate at a specified velocity. The boundary
 229 conditions for the laminate were defined as simply supported surfaces of the laminate in contact with the test

230 rig fixture system. This might not be the most accurate representation of the actual boundary conditions,
231 especially for the transient processes, but this method is assumed as reasonable.

232 For acceleration of the solution process, the entire model domain is symmetric with respect to geometry, loads,
233 and boundary conditions. Therefore, the model was split into two symmetric parts and only one of them was
234 modelled with proper symmetry conditions.

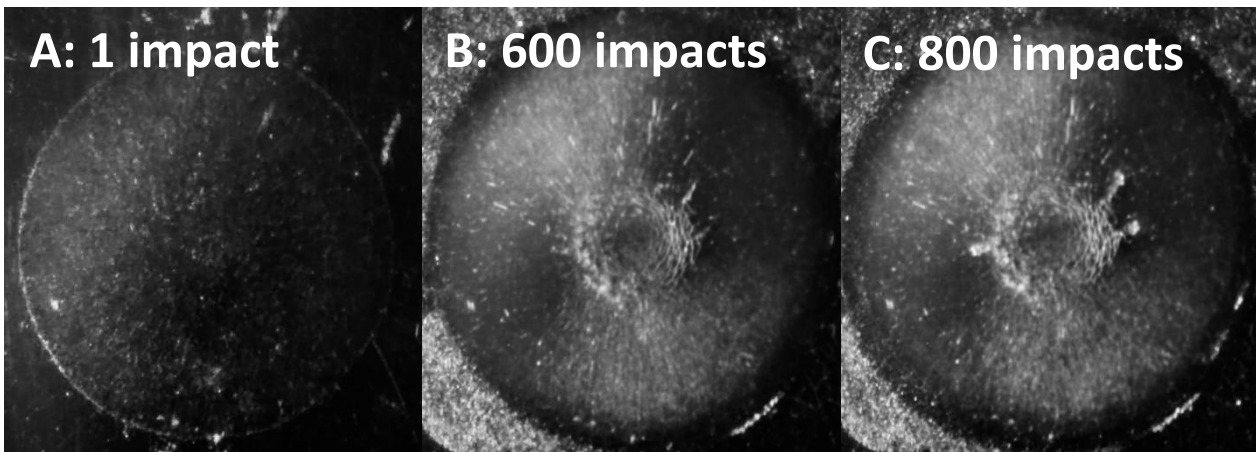
235 Since the impact transient process is fast with large stress gradients in space and stress variations in time, the
236 explicit method was used to solve the FEM model at each time step. In contrast to the implicit method which
237 is commonly used for slow quasi-static processes, the explicit method does not seek for equilibrium of the
238 system at each time step. This allows significantly faster solutions, with moderate risks for the solution to drift
239 away from the solution obtained with implicit method.

240

241 3. Results and discussion

242

243 3.1. Failure criterion by visual damage



244

245 Figure 9. Images from the in-situ video capture showing different stages of testing impact speed 129.8 ± 0.82
246 m s^{-1} at impact frequency 2Hz. A: Impacted but visually undamaged. B: Impacted sample with circular crazing
247 evident in high-stress impact region. C: Impacted sample just after first material loss denoting the end of
248 incubation time.

249

250 One of the advantages of SPIFT is that it allows simple in-situ damage assessment. In conventional RET, the
251 rotating target, in a rain and water mist environment, makes the capture of high-resolution images difficult.
252 Therefore, high-resolution imaging is usually performed outside the RET setup.

253 Since samples used in SPIFT are stationary, high-quality image or video capture is a relatively simple task and
254 is achieved using the camera described in section 2.4.

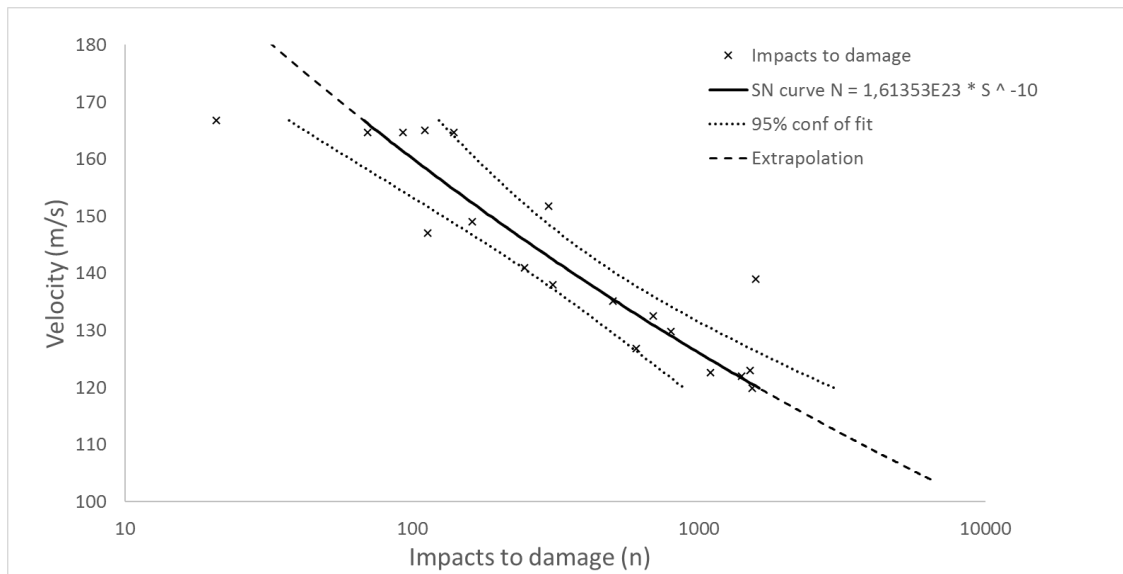
255 From the captured visual data the incubation time was identified. End of incubation was determined by the
256 time at which the first material loss is observed denoting the onset of constant erosion (see Figure 9). In Figure
257 9, the image B exemplifies a sample close to the end of incubation, where a part of the coating is about to be
258 detached from the laminate. Hereafter, the partial removal of the coating is referred to as “damaged”.

259 Depending on the test conditions, the incubation time could be determined within 2-20 impacts. The higher
260 the impact speed, the more abrupt the change from un-damaged to damaged, whereas at lower impact speeds
261 the change was less abrupt. As seen in Figure 9, circular crazing is observed prior to erosion, and is consistent

262 across all samples. These circular cracks bear a strong resemblance to literature [15], in which the MIJA
263 (Multiple Impact Jet Apparatus [16]) was used to induce erosion in carbon nanotube reinforced polymers. The
264 fact that the crazing starts away from the point of impact is due to peak stress intensity coupled with the specific
265 material properties of both projectile and target, as well as the impact speed.

266 The crazing is analysed further in section 3.4 and 3.5 where X-ray tomography and FEM modelling are
267 combined to show a correlation between stress waves and crack propagation.

268 The data pairs (impacts to end of incubation, speed) are plotted in an SN or Wöhler diagram shown in Figure
269 10, where traditionally the independent parameter, velocity, is plotted on the vertical axis and the dependent
270 parameter, number of impacts before visible erosion, is plotted on the horizontal axis of a semi log. Such a
271 representation of data is known from fatigue testing of materials [17], where the number of load cycles causing
272 damage is shown as a function of the magnitude of each load cycle (for example stress range). The fatigue data
273 are fitted with a power function as shown in Figure 10.



274
275 Figure 10. Semi-Log plot showing number of impacts to end of incubation at a set impact velocity fitted to a
276 power curve.

277

278 3.2. *Experimental results from AE*

279 After running several SPIFT series with AE sensing, it became apparent that a significant change was occurring
280 in the recorded AE signal for impact events at the immediate point where the coating was visibly damaged
281 (see image C in Figure 9). An example of the AE feature read-outs generated during one of these test series is
282 shown below.

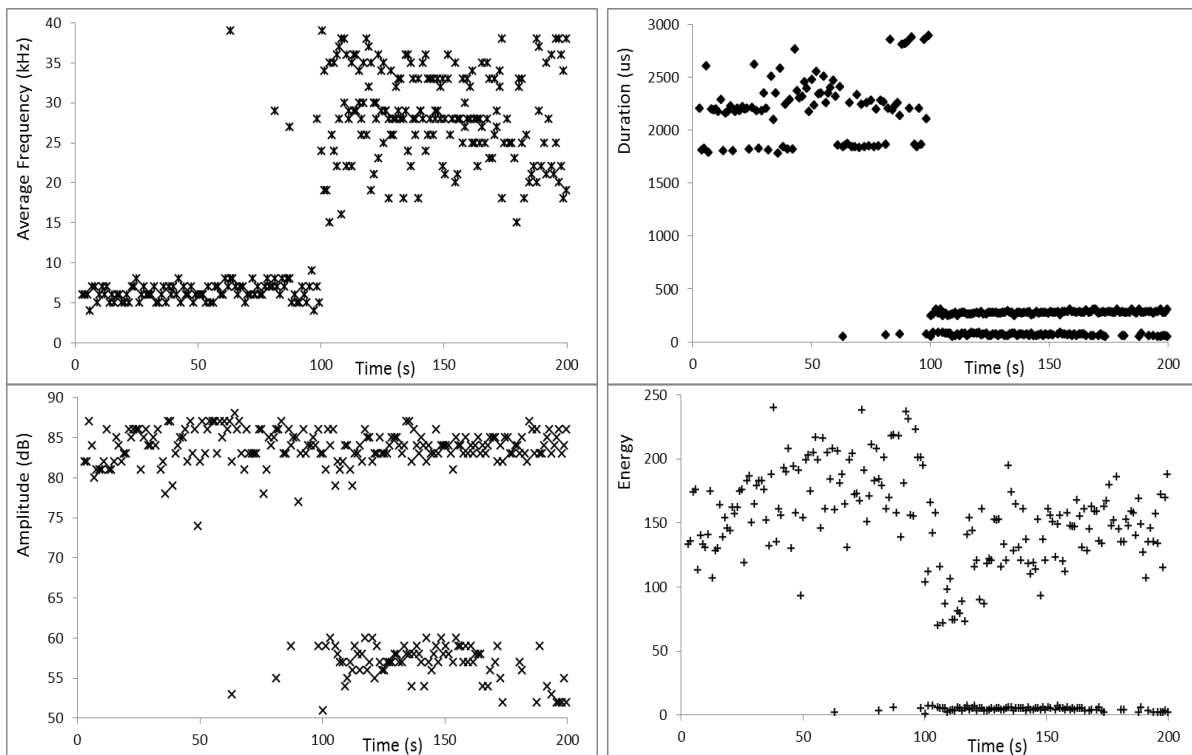
283 Figure 11 shows a sharp change in average frequency of the AE hits recorded during the SPIFT series occurring
284 at the point when the coating started to erode from the surface of the specimen. The group of hits from before
285 this point (coating intact) is distinct from the group of hits recorded afterwards (coating eroded).

286 Figure 11 also shows that there is a change in amplitude of the AE hits recorded during the SPIFT series at the
287 point when the coating is eroded from the surface of the specimen. In this case, the eroded coating results in
288 multiple hits being recorded for each rubber ball impact, similar to the problem described in section 2.5.
289 Ignoring these low amplitude secondary hits there is not a large change in amplitude following initial visible
290 coating damage.

291 There is, however, a very significant change in duration of the AE hits recorded during the SPIFT series at the
292 point where the coating becomes visibly damaged.

293 A change in the energy of each AE hit recorded during the SPIFT series is observed at the point where the
294 coating is visually seen to be damaged. What is also apparent from this feature is that a progression can be
295 observed in the energy extracted from the AE hits as the impact series goes on. The energy content of the
296 individual hits seems to be increasing up until the point where the coating is damaged when a step change
297 (downwards) takes place. Following this, a similar progression of increasing energy for the individual AE hits
298 is again observed.

299



300

301 Figure 11. AE features during a typical SPIFT series at impact rate of 1 Hz; the coating is eroded after 100 s.

302

303 Summarising these changes in Table 3, we can see that when the coating is damaged, the average carrier
304 frequency of the AE hit waveform increases, the maximum amplitude of the hits remains the same, the duration
305 of each individual AE hit decreases sharply, and the total energy contained in the AE waveform goes down
306 slightly.

307 It may seem counterintuitive that the energy recorded by the sensor on the reverse of the SPIFT specimen
308 should decrease for each rubber ball impact once the coating is removed. But it is important to bear in mind
309 that the energy feature of the AE waveform returns the energy content of the entire waveform detected but
310 says nothing about the morphology of that waveform. The energy content of each detected AE waveform is
311 related to the area above the threshold voltage and under the shape described by the waveform. Note that as
312 soon as the coating is damaged, the duration of the waveforms detected is seen to be sharply reduced while the
313 maximum amplitude remains the same.

314 If we consider how much energy is being transferred into the laminate where the AE sensor is attached as a
 315 function of time we can divide the energy content of each hit detected by it's waveform duration.

316

317 Table 3. AE features average value change after coating erosion.

AE waveform characteristic	hits prior to initial visible damage		hits after initial visible damage	
	mean	St.dev.	Mean	St.dev.
Av- Frequency (kHz)	7	71%	25	16%
Amplitude (dB)	83	7%	84	2%
Duration (μs)	2123	24%	277	5%
Counts	13	23%	7	14%
Energy	167	27%	135	21%

318

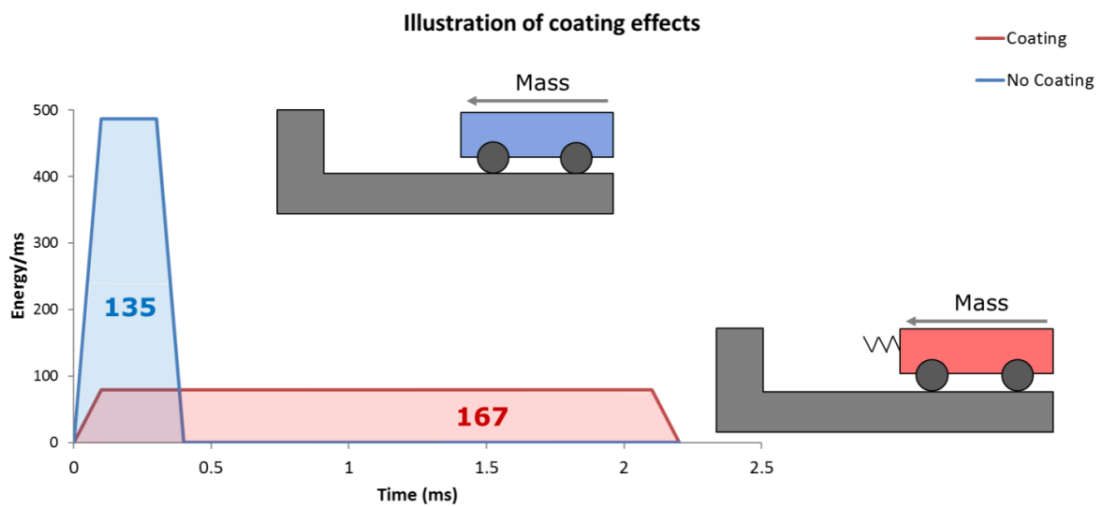
319 Table 4. Energy per unit time calculation.

	Energy	Duration (ms)	Average energy per millisecond
Average AE hit when the coating is intact	167	2.123	79
Average AE hit after initial coating damage	135	0.277	487

320

321

322 The average energy per unit time for each rubber ball impact before the coating erosion is 79 units per ms, and
 323 after the coating is removed this goes up to 487 units per ms. The result is a significant increase ($\times 6$) in the
 324 strain rate experienced by the bulk laminate following the erosion of the coating.



325

326 Figure 12. Coating effects illustration, comparison to crumple zone.

327

328 Illustrating the phenomena visually in Figure 12, we can see that although the hits on the specimen when the
 329 coating is intact contain slightly more absolute energy, this energy is distributed over a significantly longer
 330 period of time (over 2 ms) at a rate of 79 units of energy per ms. Whereas the hits when the coating is removed
 331 record energy at a rate of 487 units of energy per ms for slightly less than 0.3 ms total duration.

332 In this way, the coating on the laminate specimen acts like a crumple zone in a car subjected to impact. The
333 energy transferred from a moving object striking a stationary object is the same, but the crumple zone design
334 of the car ensures that this energy is distributed in time, thus saving the occupant from a potentially deadly
335 deceleration.

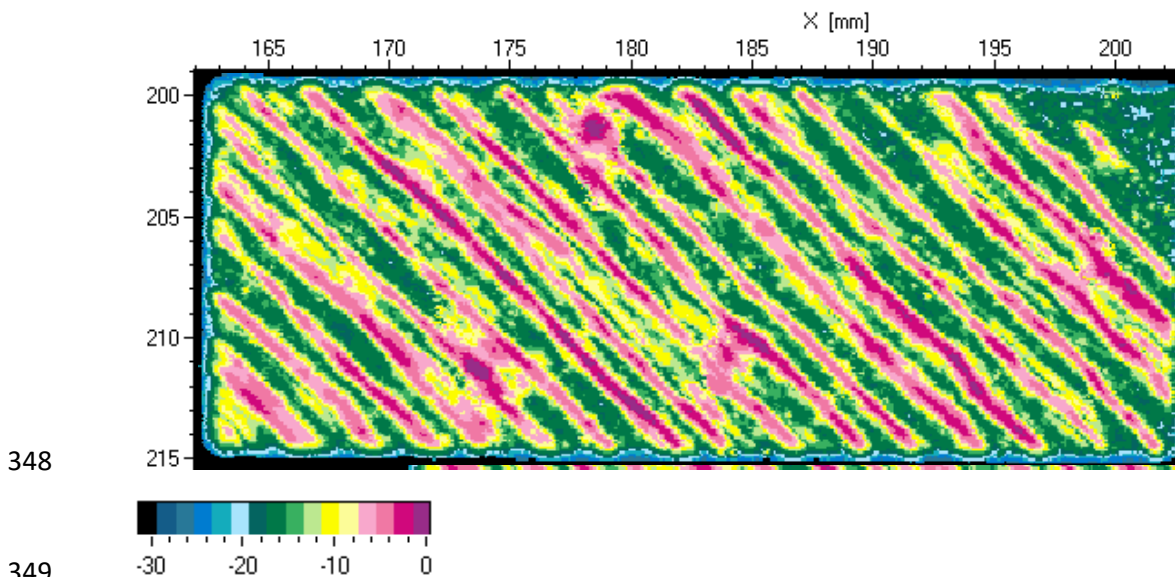
336 From the initial measurements of AE on SPIFT test series, we can confirm that it is possible to detect changes
337 in the recorded AE signal that corresponds to the damage condition of the coating and laminate. It appears to
338 be possible to classify the types of AE waveforms from each impact to determine if the coating is functioning
339 acceptably, if the coating is not performing as it should, and if the coating has been removed.

340

341 3.3. *Ultrasound*

342 Specimens were scanned both before and after they were exposed to impact damage.

343 In Figure 13 a specimen was scanned before impact test. Reflection of ultrasonic waves happens when there
344 is a change in acoustic impedance Z . Using common values [9] for impedance Z of epoxy resins of between
345 $1.7\text{-}2.4$ (MPa s m^{-1}) and glass fibres $13.3\text{-}14.5$ (MPa s m^{-1}), it is clear that there is a significant difference in
346 impedance between the two materials. It is concluded in Figure 13 that the high signal area (yellow-magenta
347 lines) is the reflected signal form the first layer of fibres (45° oriented).

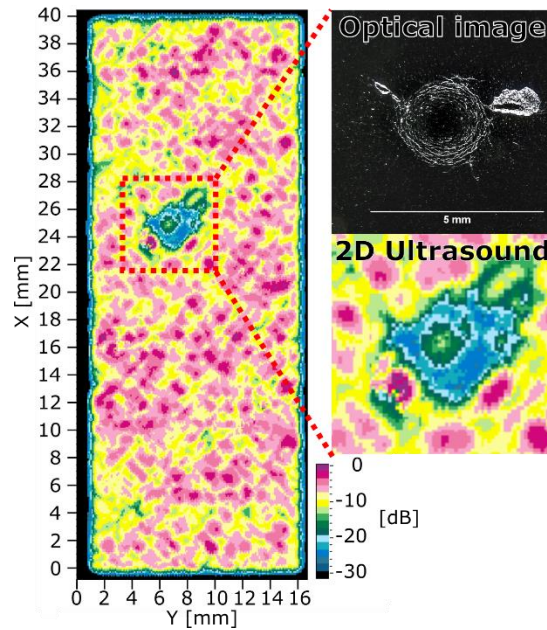


350 Figure 13. Ultrasonic scan from a specimen without impact damage (Specimen EMB-02). The 45° rovings of
351 the upper ply show as lines of low damping in the scan.

352

353 In Figure 14 the specimen was scanned after 140 impacts at 164 m s^{-1} . The scan shows the impacted area.

354 Looking closer at Figure 14 there is a circular area of light blue signal with a diameter of roughly 3mm. Despite
355 the sample having clear surface erosion damage, it is the area that shows circular crazing but no surface erosion
356 that influences the ultrasound scan most. Many factors can lower the strength of the reflected signal but likely
357 candidates are reflection or diffuse reflection of the incoming ultrasound signal as shown in Figure 7 in section
358 2.6.



359

360 Figure 14. Scan from the specimen with impact damage from air gun overlaid with a visual image of the
 361 damaged sample. In the impacted area, there is a clear loss of signal compared to the surrounding area that
 362 shows the crosshatch pattern from the first and second glass fibre layers.

363

364 From the CT-scan in section 3.4 below, there are conical cracks can reduce the reflected signal. This reduced
 365 signal is likely a result of incoming ultrasound signal reflected away from the transducer due to the 45° cracks
 366 in the impacted region. With a impedance of around $0.43 \cdot 10^{-3} \text{ MPa} \cdot \frac{\text{s}}{\text{m}}$ any air gap inside the conical cracks
 367 will result in a strongly reflected signal.

368 Using ultrasound scanning in this way provides a good nondestructive tool to quickly access the presence or
 369 extent of damage resulting from impact with typical scan times ranging between 5-10 min. This makes it an
 370 ideal first analysis tool before applying more expensive and time-consuming methods like CT-scanning.

371 By scanning laminates between impact series, the development of damage can be followed non-destructively.
 372 This applies not only to the SPIFT setup but, if correctly implemented, could also be adapted to the curved
 373 whirling arm RET specimens, either by just scanning the part of the leading edge parallel to the transducer, or
 374 by mounting the transducer to the specimens, capable of following the surface contour.

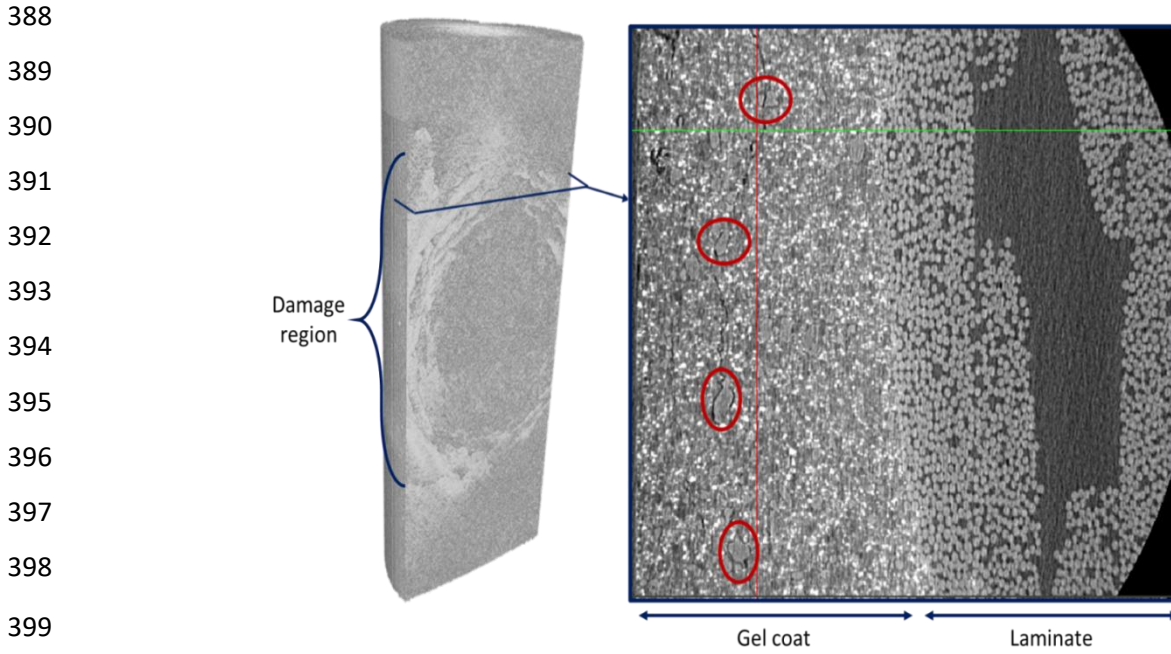
375

376 3.4. 3D X-ray tomography

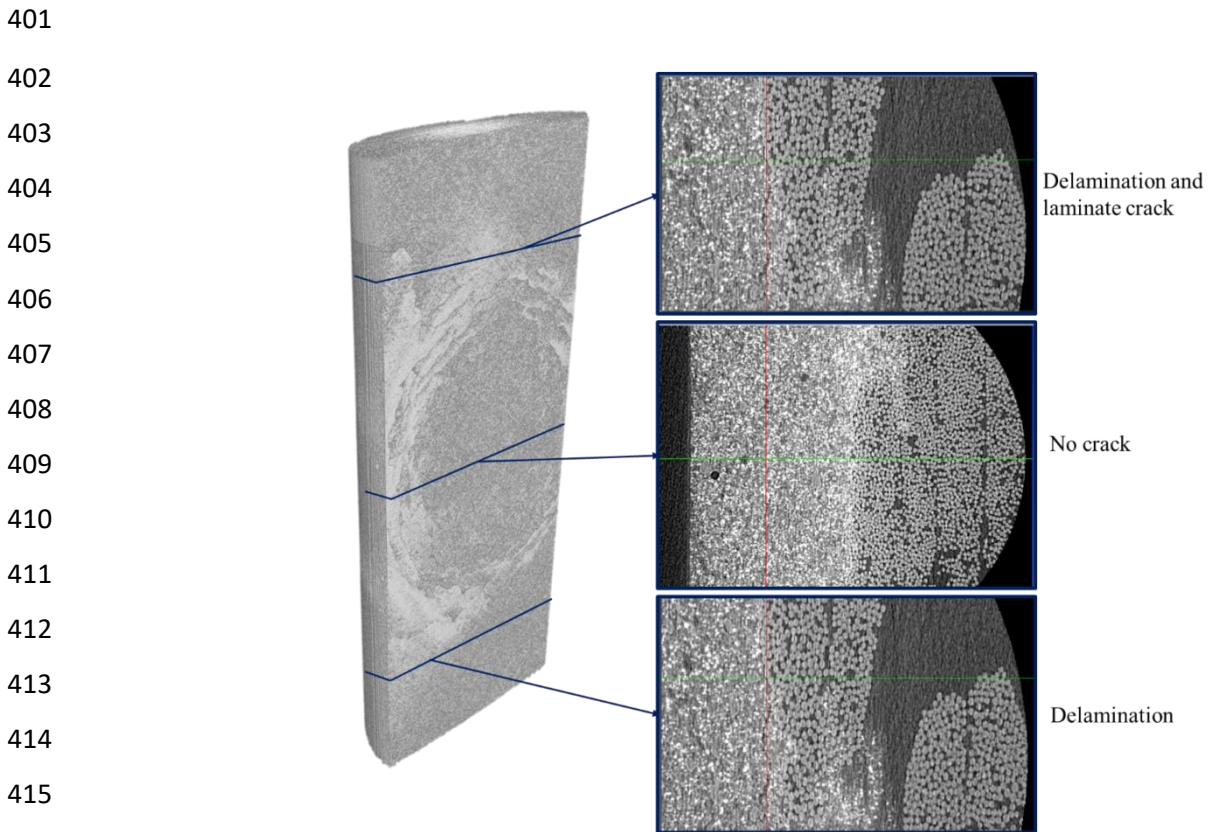
377 Damage mechanisms can be identified and followed using the 3D X-ray tomography. Figure 15 shows a 3D
 378 volume of the tested specimen. This scan is a superposition of three smaller scans (each 2 mm³). This procedure
 379 is called stitching and permits the study of a large volume with a small pixel resolution. The impact area is
 380 clearly observed and its diameter can be measured. It is found that several circular cracks were formed around
 381 the impact area.

382 First, the damage mechanisms appearing during single point impact fatigue need to be investigated in order to
 383 understand the failures. The observation indicates that this particular gelcoat includes large particle fillers that
 384 appear to be responsible for the crack initiation which occurred before visual damage of the partial coating
 385 removal. The fillers are acting as stress concentrating defects which facilitate the crack propagation within the

386 material (Figure 15). The total diameter of the damage region is 2.3 mm to 3.0 mm for this specific gelcoat
387 material.



400 Figure 15. Damage mechanism in the gelcoat. Damaged region: 2.3-3.0 mm.



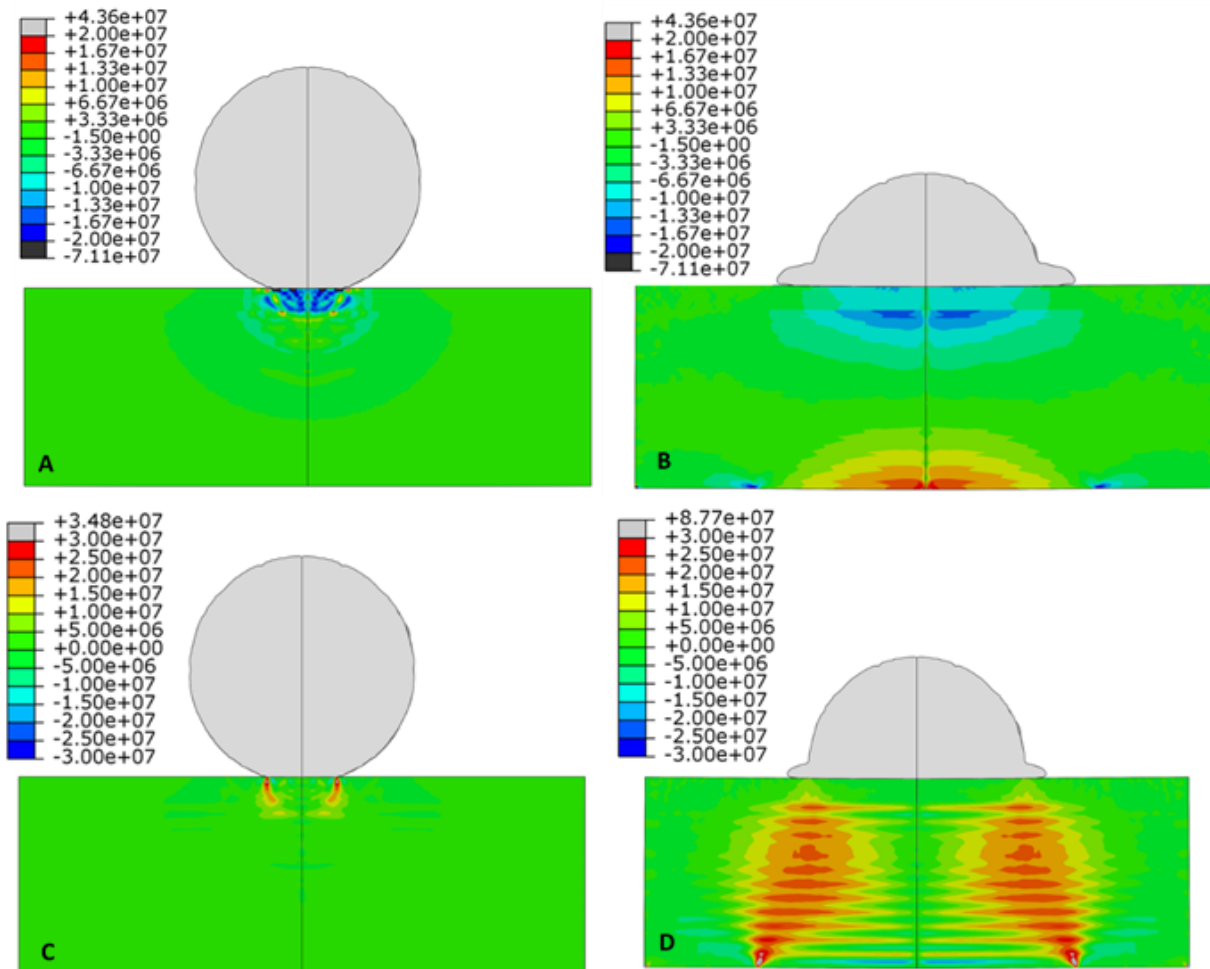
417 Figure 16. Damage localisation in the impact region.

418 A further study of the entire impact zone reveals an interesting phenomenon. At the centre of the impact zone,
 419 no cracks are identified in the gelcoat. Near the centre of the impact zone, there are no or only a few cracks.
 420 Moving from the centre towards the rim, the first cracks appear at around 75% of the outer diameter, and they
 421 increase in density near the edge of the zone. The cracks are ring-shaped at the surface of the gelcoat, and they
 422 extend into the gelcoat at an angle of 45° thus forming cone shaped crack surfaces. Outside the impact, cracks
 423 are running closer to the interface; delamination can be identified in this region (Figure 16). The conic shape
 424 of the impact cracks through the gelcoat thickness is to be expected and has been observed in other materials
 425 subjected to impact.

426

427 3.5. *FEM results*

428



429

430 Figure 17. Stresses in the laminate under nitrile ball impact. A and B: σ_{11} stress at the transient (5 μ s), and
 431 quasi static stage (21 μ s). C and D: σ_{13} stress at the transient and quasi static stage.

432

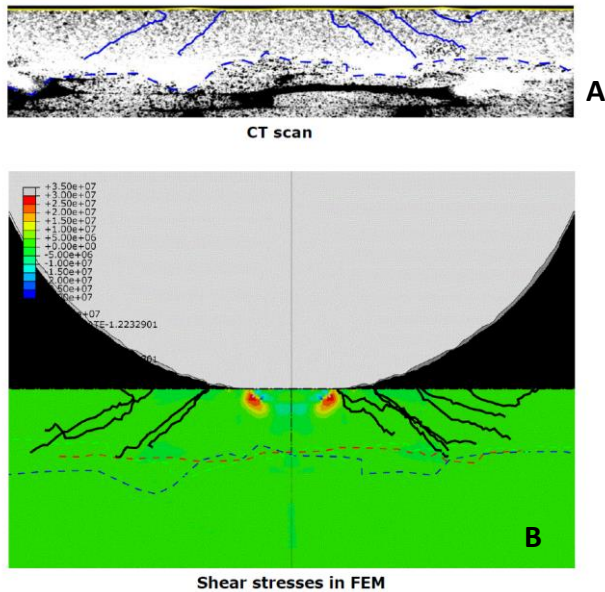
433 The results of the simulations in tensile stress are shown in Figure 17. It can be seen that while at the beginning
 434 (transient stage of the impact), the highest stress is localised under the contact surface, at the quasi-static stage
 435 the high stress region forms in the depth under the surface. Similarly, rather high shear stresses form at the
 436 angle 30° to 45° under the contact surface.

437 Further, the comparison between the laminate deformation under rubber ball and water droplet impacts have
438 been carried out (at the loading rate 80 m s^{-1}). It was observed that the shear stresses in the laminate are 70%
439 higher under the water drop (17 vs 10 MPa) than under the rubber ball.

440 The results of simulations have been compared with experiments. CT scanning of the specimens revealed
441 cracks in gelcoat at 30 to 45° relative to the surface as shown in Figure 18. The cracks observed in the scan are
442 in agreement with the FEM simulation the shear stresses is also presented.

443

444



445

446 Figure 18. Comparison of the cracks observed in CT scan and the shear stress distribution as well as
447 delamination between the laminates and coating represented by the dashed lines. The blue lines in Figure A are
448 drawn on top of the observed cracks and superposed in B together with lines coming from two more tested
449 samples.

450

451 4. Conclusion

452

453 Experimental and theoretical assessments for damages caused by repeated high speed impacts were presented.
454 SPIFT demonstrated repeated impacts on a coated laminate with rubber balls, damaging the coating and the
455 laminate. In-situ video observation and AE monitoring and ex-situ characterisations by ultrasonic scanning
456 and X-ray CT-scan were carried out.

457 In-situ video data enabled determination of the incubation time and plotting of SN curves in terms of coating
458 removal at an impact speed ranging between 123 and 165 m s^{-1} . It is demonstrated that the incubation time
459 obtained by the video observation showed correlation to the change of AE signal recorded in the in-situ AE
460 data. The ex-situ characterisations by ultrasound and CT scans revealed that damage could be induced in the
461 coating and the laminate before the visible damage started. In particular, the ex-situ CT scans were capable of
462 identifying conical cracks in the coating resulting from the repeated impacts. Additional repeated impacts
463 extended the cracks into the laminate. An FEM model indicated intense shear-stress components, showing a
464 good agreement with the coating cracks observed with the CT-scans.

465 The techniques presented can be used for studying high speed impact damages, in particular, leading edge
466 erosion of wind turbine blades. The in-situ methods demonstrated immediate detection of changes and damages
467 while the ex-situ methods as well as the modelling can provide dedicated analysis. It is therefore suggested
468 that combination of these techniques will enable efficient investigation of the complicated high speed impact
469 damage processes that can be seen in reality, for example, in the leading edge erosion of wind turbine blades.

470

471 **Acknowledgements**

472

473 The authors are grateful to Lars Lorentzen for developing SPIFT, Erik Vogeley for operation of the X-ray CT-
474 scan, and Christian H. Madsen and Jonas K. Heininge for fabricating laminate specimens. This research was
475 partly supported by EUDP project ‘Rain erosion tester for accelerated test of wind turbine blades’, Case no.:
476 64015-0045 (EUDP) and the Innovation Fund Denmark being part of the Fast-Track consortium (5152-
477 00002B). This research was conducted using mechanical testing equipment from Villum Center for Advanced
478 Structural and Material Testing (CASMAT), award reference 00007293 from Villum Fonden.

479

480 **References**

- 481 1. *Progress and recent trends of wind energy technology*. **M.R Islam, S. Mekhilef, R. Saidur**. s.l. : Renewable
482 Sustainable Energy Rev., 2013, Vol. 21. 456-468.
- 483 2. *The evolution of wind turbine design analysis—a twenty year progress review*. **D.C Quarton** s.l. : Wind
484 Energy, 1998, Vol. 1. 5-24.
- 485 3. *Why offshore wind energy?* **M.D Esteban, J. Diez, J. S. Lopez, V. Negro**. s.l. : Renewable Energy, 2011,
486 Vol. 36. 444-450.
- 487 4. *The wind energy (r)evolution: A short review of a long history*. **J.K Kaldellis, D. Zafirakis**. s.l. : Renewable
488 Energy, 2011, Vol. 36. 1887-1901.
- 489 5. *Wind Turbines: How Big can they Get?* **G. Marsh**. s.l. : Refocus, 2005, Vol. 6. 22-28.
- 490 6. **C. Red**, *Composites Technology*. s.l. : Composites World, Web Publisher, 2008.
- 491 7. *On erosion issues associated with the leading edge of wind turbine blades*. **M.H Keegan, D.H Nash, M.M**
492 **Stack**. s.l. : J. Phys. D Appl. Phys., 2013, Vol. 46. 383001.
- 493 8. *Computational analysis of wind turbine blade erosion*. **A.Castorrini, A. Corsini, F. Rispoli, P. Venturini, K.**
494 **Takizawa, T.E Tezduyar**. s.l. : Computers and Fluids, 2016, Vol. 141 175-183.
- 495 9. *Leading Edge Erosion of Coated Wind Turbine Blades: Review of Coating Life Models*. **H.M Slot, E.R.M.**
496 **Gelinck, C. Rentrop, E. Van der Heide**. s.l. : Renewable Energy, 2015, Vol. 80. 837-848.
- 497 10. *Rain erosion of wind turbine blade coatings using discrete water jets: Effects of water cushioning,*
498 *substrate geometry, impact distance and coating properties*. **S. Zhang, K. Dam-Johansen, P.L. Bernad Jr, S.**
499 **Kiil**. s.l. : Wear, 2015, Vols. 328-329 140-148.
- 500 11. **2012, ASTM**. *ASTM G73- Standard Test Method for Liquid Impingement Erosion Using Rotating*
501 *Apparatus*. 2012.

- 502 12. *Impact fatigue damage of GFRP materials due to repeated raindrop collisions.* **G. Prayogo, H. Homma,**
503 **T. P. Soemardi, A.S. Danardono.** s.l. : Trans . Indian Inst. Metals, 2011, Vols. 64 (4-5). 501-506.
- 504 13. *Cumulative fatigue damage and life prediction theories: a survey of the state of the art for homogeneous*
505 *materials.* **A. Fatemi, L. Yang.** s.l. : Int. J. Fatigue, 1998, Vol. 20(1). 9-34.
- 506 14. *Cumulative Damage in Fatigue.* **K. Reifsnider, S. Case, J. Duthoit.** s.l. : Composites Sci. Technol., 2000,
507 Vol. 60. 2539-2546.
- 508 15. *Multiple Liquid Impacts on Polymeric Matrix Composites Reinforced with Carbon Nanotubes.* **O.**
509 **Gohordani, D.M. Williamson, D.W. Hammond.** s.l. : Wear, 2012, Vols. 294-295. 336-346.
- 510 16. *Multiple Impact Jet Apparatus (MIJA): Application To Rain Erosion Studies.* **P.N.H. Davies, J.E. Field.** s.l. :
511 Proc. SPIE 1112, Window and Dome Technologies and Materials, 1989. Vol. 1112. doi: 10.1117/12.960790.
- 512 17. *Estimation of fatigue curves for design of composite laminates.* **K.O. Ronold, A.T. Echtermeyer.** s.l. :
513 Composites A, 1996, Vol. 27. 485-491.
- 514 18. *A review of wind energy technologies.* **G.M Herbert, S. Iniyar, E. Sreevalsan, S. Rajapandian.** s.l. :
515 Renewable Sustainable Energy, 2007. Vol. 11 (6) 1117-1145.
- 516 19. [Online]
517 [http://www.physicalacoustics.com/content/literature/multichannel_systems/Express_8_Product_Bulletin.](http://www.physicalacoustics.com/content/literature/multichannel_systems/Express_8_Product_Bulletin.pdf)
518 pdf.
- 519 20. [Online] http://www.physicalacoustics.com/content/literature/sensors/Model_Nano30.pdf.
- 520 21. *Leading edge erosion of coated wind turbine blades: Review of coating.* **H.M. Slot, E.R.M. Gelinck, C.**
521 **Rentrop, E. van der Heide.** s.l. : Renewable Energy, 2015. Vol. 80. 837-848.
- 522